1-1-2019

Oxygen vacancies promoting the electrocatalytic performance of CeO 2 nanorods as cathode materials for Li-O 2 batteries

Yue Hou
Shandong University

Jun Wang
Shandong University, jw707@uowmail.edu.au

Chuanxin Hou
Shandong University

Yuqi Fan
Shandong Normal University

Yanjie Zhai
Shandong University

See next page for additional authors

Oxygen vacancies promoting the electrocatalytic performance of CeO 2 nanorods as cathode materials for Li-O 2 batteries

Abstract

Li-O 2 batteries have become very promising power sources for electronic vehicles as a result of their extraordinary energy density. Nevertheless, the unfavourable electrocatalytic activity of cathode materials in Li-O 2 batteries is still a limiting factor for the practical application of Li-O 2 batteries. This study proposes a surface engineering strategy which can enhance the electrocatalytic activity of CeO 2 nanorods by tuning the oxygen vacancies on their surface, and found that the highest concentration of oxygen vacancies induces the best electrochemical performance, including an extended electrochemical stability of 200 cycles, and reduces the overpotential of the ORR from the reported 0.26 V to 0.11 V. Ex situ XPS photoelectron spectroscopy was carried out to further explain the role of oxygen vacancies in improving the electrochemical performance of LOBs, indicating that the oxygen vacancies of CeO 2 nanorods have more obvious positive effects on the ORR than on the OER. It is believed that they can serve as the active sites for the deposition of Li 2 O 2 films by being involved in the reaction between Li + and O 2 during the ORR, and also boost the electron transport through the insoluble Li 2 O 2 films to further catalyse the Li + and O 2 reaction during the discharge and charge process. This work provides new proof for the association between the discharge/charge behaviour of LOBs and the content of oxygen vacancies.

Disciplines

Engineering | Physical Sciences and Mathematics

Publication Details

Hou, Y., Wang, J., Hou, C., Fan, Y., Zhai, Y., Li, H., Dang, F. & Chou, S. (2019). Oxygen vacancies promoting the electrocatalytic performance of CeO 2 nanorods as cathode materials for Li-O 2 batteries. Journal of Materials Chemistry A, 7 (11), 6552-6561.

Authors

Yue Hou, Jun Wang, Chuanxin Hou, Yuqi Fan, Yanjie Zhai, Hongyu Li, Feng Dang, and Shulei Chou

Journal Name

ARTICLE

Oxygen Vacancies Promoting the Electrocatalytic Performance of the CeO_2 Nanorods as the Cathode Materials for Li-O_2 Batteries

Received 00th January 20xx,
Accepted 00th January 20xx

DOI: 10.1039/x0xx00000x

www.rsc.org/

Yue Hou,[a,‡] Jun Wang,[a,‡] Chuanxin Hou,[a] Yuqi Fan,[b] Yanjie Zhai,[a] Hongyu Li,[a] Feng Dang,[a*] Shulei Chou[c*]

The Li-O_2 batteries have become very promising power for electronic vehicles as a result of their extraordinary energy density. Nevertheless, the unfavourable electrocatalytic activity of cathode materials in Li-O_2 batteries is still a limited factor for the practical application of Li-O_2 batteries. This study proposes a surface engineering strategy which can enhance the electrocatalytic activity of CeO_2 nanorods by tuning oxygen vacancies on their surface, and found that the highest concentration of oxygen vacancy induces the best electrochemical performance, including extended electrochemical stability of 200 cycles, and inducing the overpotential of ORR from the reported 0.26 V to 0.11 V. The ex-situ XPS photoelectron spectroscopy was carried out to further explain the reaction mechanism of oxygen vacancies in improving electrochemical performance for LOBs, indicating that the oxygen vacancies of CeO_2 nanorods have more obviously positive effects on ORR than OER. It is believed that they can serve as the active sites to the deposition of Li_2O_2 films by being involved in the reaction between Li^+ and O_2 during ORR, and also boost the electron transport through the insoluble Li_2O_2 films to further catalyse the Li^+ and O_2 reaction during discharge and charge process. This work provides a new proof into the association between the discharge/charge behaviour of LOBs and the content of oxygen vacancies.

Introduction

Li-O_2 batteries (LOBs) have triggered worldwide attention owing to their high theoretical energy density and specific capacity, which is the key to satisfy the requirement for researching next-generation power supply system. However, the wide spread use of LOBs has been impeded by several limitations, for example, a lower-than-expected capacity, quite high overpotential during the discharge/charge process, low efficiency of energy conversion and lack of cycle stability.[1-5] These shortages are highly related to the low-efficiency reversible formation of the Li_2O_2 films.[6, 7] During the discharge process, the surface of the cathode can be continuously covered by the insoluble Li_2O_2 films, which can induce the low electronical conductivity and thus enhance the decomposition energy barrier of the Li_2O_2 films, leading to the high overpotential and poor cyclability. To tackle this problem, a lot of efforts have been paid to explore catalytic materials possessing outstanding electro-catalytic activity to improve the electrochemical reactions, such as precious metals[8, 9], metal alloys[10, 11], metal oxides[12-14], porous carbon[15-17] and metal carbide[18, 19]. Transition-metal oxides (TMOs, including TiO_2, Co_3O_4, MnO_2, etc.) have raised much attention of the researchers because of their low cost and high catalytic efficiency. It is, however, still challenging to enhance their ORR and OER activity of LOBs by employing TMOs as the cathode catalysts.

Recent studies have proposed that the catalytic performance of TMOs can be affected by the surface structure and interface interactions between supports and catalysts, which can be improved by adjusting the atoms distributing on the surface or valence distribution.[20-25] Therefore, many researchers have been devoting to develop new strategies to improve the electrocatalytic activity of TMOs, like tuning the surface atom or electronic structure through doping heteroatom, vacancy engineering, and exposed optimal crystal plane.[26-28] The introduction of oxygen vacancies is one of the effective strategies. This is because they cannot only lower the reaction energy barrier of reversibly decomposing discharge products, but also accelerate electron transport, which can play a positive part in boosting ORR between Li^+ and O_2 occurring at the Li_2O_2 interface of the electrode through the previously formed Li_2O_2 films and serve as active sites where the preferential reaction between the Li^+ and O_2 occurred. Wang et. al. proposed that electrochemical performance of LOBs can be enhanced by tuning the inner oxygen vacancy concentration when Co_3O_4 nanosheets serve as cathode catalysts, which proven that the discharge specific capacities of Co_3O_4 nanosheets exhibited an increment of 10 times more than that of bulk Co_3O_4, with prolonged cycle life of about 100 cycles[23] Chen et. al. found that the generation of oxygen vacancies

[a] *Key Laboratory for Liquid-Solid Structural Evolution and Processing of Materials (Ministry of Education), Shandong University, Jinan 250061, P.R. China*
[b] *Institute of Environment and Ecology, Shandong Normal University, Jinan 250014, China*
[c] *Institute for Superconducting and Electronic Materials, University of Wollongong, Squires Way, North Wollongong, NSW 2500, Australia*
E-mail: dangfeng@sdu.edu.cn
‡ These authors contributed to this work equally.
Electronic Supplementary Information (ESI) available: [details of any supplementary information available should be included here]. See DOI: 10.1039/x0xx00000x

Please do not adjust margins

could boost the ORR activity of MnO_2.[29] It is reported by Zhang et. al. that $MoO_{3-x}NS_{s-2}$ owing high-content oxygen vacancies shows the best electrocatalytic activity, which enables the electrochemical performance for cathode achieve a leap, including a lower overpotential of about 0.5 V and a longer stable cycle life over 60 cycles.[30] Similarly, Lee et. al. prepared $Na_{0.44}MnO_2$ catalyst with oxygen vacancies on their surface, which shows a higher discharge potential and about 280 mV lower charging potential.[31] In terms of these experiments, oxygen vacancies were beneficial to improving the electrocatalytic activity of TMOs and further achieve better electrochemical performances of LOBs, because they can serve as active sites for binding intermediate products, and boost electron transportation in the Li_2O_2 films.

Among various TMOs, Ceria(CeO_2) has been also studied as catalytic active species,[32] promoters and supports for catalysis,[4] solid oxide fuel cells,[33] environmental remediation[34] and heterogeneous organic synthesis[35] over the past decades. For these applications, one of the distinct features of CeO_2 is its non-stoichiometry, expressed by the presence of Ce^{4+} ions reduced to Ce^{3+} ions and oxygen vacancies, which could be transferred on its surface.[36, 37] Some previous results proposed that the catalytic ability of CeO_2 could be largely depended on the ratio of surface Ce^{3+}/Ce^{4+} and the content of oxygen vacancies.[38, 39] Owing to the easy shift between oxidized and reduced states and the highly efficient adsorption of superoxide radicals, CeO_2 has been considered as one of the best promising catalyst candidates for promoting both the ORR and the OER in LOBs.[40-42] CeO_2 have been explored in lots of work on the cathodes for LOBs, serving as not only a catalyst but also an "oxygen pump" to relieve oxygen insufficiency during the ORR.[43, 44] However, the role of oxygen vacancies playing in improving the electrochemical performance of LOBs is still unravelled.

In this work, we carried out the ex-situ X-ray photoelectron spectroscopy to investigate the four typical states of the cathode to further explain the reaction mechanism of oxygen vacancies in improving electrochemical performance for LOBs. Firstly, we proposed a strategy to improve the electro-catalytic activity of porous CeO_2 nanorod cathode for LOBs by tuning the content of oxygen vacancies, which can be regulated through controlling the hydrothermal temperature of the two-step hydrothermal treatment. It was revealed by experimental results that the highest concentration of oxygen vacancy induces the best electrochemical performance, including extended electrochemical stability of 200 cycles. We found that the oxygen vacancies of CeO_2 nanorods play an important role in boosting ORR, reducing the overpotential of ORR from 0.26 V to 0.11 V, and also prolonging the cycle life of LOBs, because oxygen vacancies can facilitate the electron transport through Li_2O_2 films to catalyse the reaction between Li^+ and O_2 during discharge process and charge process, and also catalyse the deposition of Li_2O_2 films as the active sites involved in the reaction between Li^+ and O_2 during discharge process. This work provides a new proof into the association between the discharge/charge behaviour of LOBs and the content of oxygen vacancies.

Experimental

Synthesis of nanorods CeO_2 (NR@CeO_2). Firstly, 10 mL deionized water was prepared to dissolve 4 mmol $Ce(NO_3)_3$ $6H_2O$, and then the above mixture was mixed with 6.86 M NaOH solution. The above solution was allowed to react at room temperature for 30 min by continuous stirring and then transferred into a stainless steel autoclave for hydrothermal treatment at 100 °C for 24 h. Afterwards, the reaction mixture was then cooled naturally to room temperature. The products were collected by centrifugation, and then thoroughly washed with ethanol and deionized water several times, which were finally dried at 60°C overnight in an oven in air. Typically, hydrothermal treatment of the precursor product at 120 °C, 160 °C and 200 °C for 12 h afforded the formation of NR@CeO_2 with different concentration of oxygen vacancies, which are designated as Ce@120, Ce@160 and Ce@200, respectively.

Physical Characterization. The images acquired from field-emission scanning electron microscope (JEOL JSM-7500F) at an acceleration voltage of 5 kV and transmission electron microscopy (JEOL JEM-2011) at an accelerating voltage of 100 kV were used to investigate the morphology of as-prepared NR@CeO_2 nanorods. Their phase composition was confirmed by X-ray diffraction (XRD) patterns which were measured on a PANalytcal X'Pert PRO instrument using Cu Kα (λ=1.5418 Å) with a scanning range of 10°-90° at a speed of 5° min^{-1}. The specific surface area of NR@CeO_2 nanorods was determined by a nitrogen adsorption-desorption method on a Micromeritics ASAP 2420 apparatus at 77 K, after being heated at 423 K under vacuum for 5 h. The pore size distribution of NR@CeO_2 nanorods was calculated by analysing the desorption branch of the isotherm tested through the NLDFT method. The X-ray photoelectron spectroscopy (XPS) measured on a PHI quantera SXM spectrometer using an excitation source of Al Kα= 280.00 eV was carried out to detect the surface electronic states of CeO_2 nanorods, and C1s peak (284.6 eV) was used as a reference peak to calibrate binding energies in order to avoid the sample charge effect.

Electrochemical Performance Measurements. To test the electrochemical performance of CeO_2 nanorod cathodes for LOBs, 40 wt.% catalyst, 40 wt.% Ketjen Black (KB) and 20 wt.% poly(tetrafluoroethylene) (PTFE) were mixed in 3 mL isopropanol to make a slurry, which was homogenously coated onto the carbon paper. Then a vacuum oven was used to dry the cathode at 120 °C for 12 h. A Li-O_2 cell includes a cathode of carbon paper loading with the catalyst, a glass fibre separator, the electrolyte made up of 1 M lithium bis(trifluoromethanesulfonyl) (LiTFSI) in tetraethylene glycol dimethyl ether (TEGDME) and a Li foil as the anode. All batteries were assembled in a glove box (Mbraun) under an Ar atmosphere (H_2O<0.1 ppm, O_2<0.1 ppm). Galvanostatic discharge/charge tests of the LOBs were implemented at room temperature on a LAND CT 2001A multi-channel battery tester in an O_2-purged chamber. The current density and specific capacity depended on the weight of catalyst in the

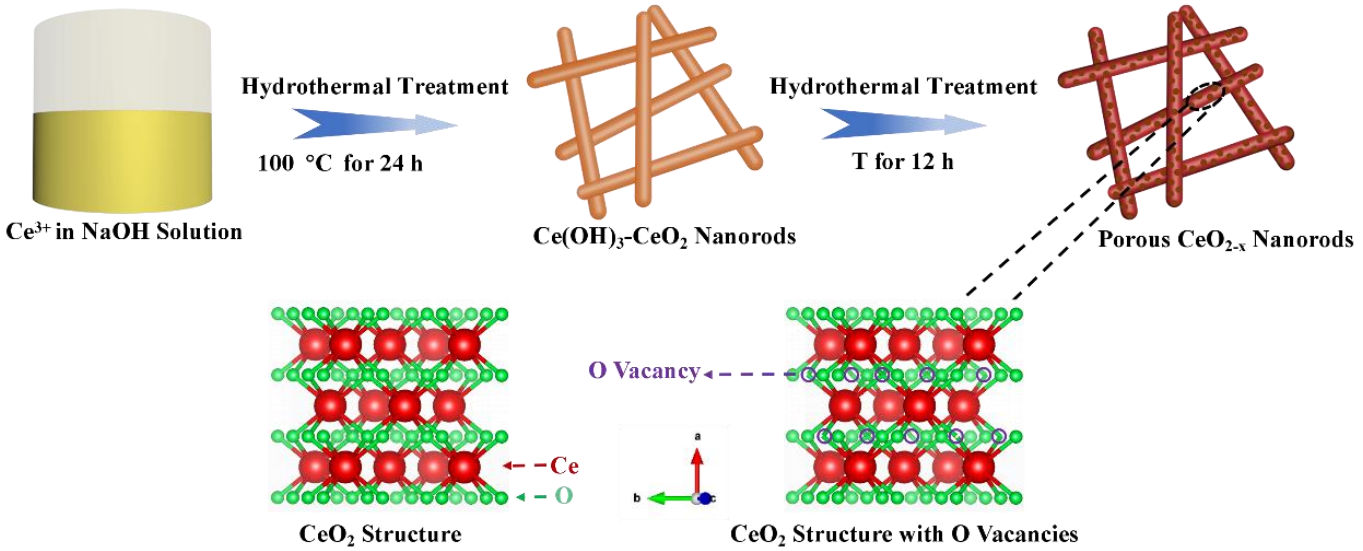

Scheme 1. Schematic representation of the procedure of synthesizing NR@CeO_2 samples, involving two hydrothermal treatment

cathodes. The cyclic voltammograms (CV) were tested at a scan rate of 0.1 mV s^{-1} in the potential range of 2.35 to 4.5 V vs. Li/Li^+ to investigate the kinetic electrochemical behaviours. And the electrochemical impedance spectroscopy (EIS) of the LOBs was evaluated within the frequency ranging from 10^5 Hz to 0.1 Hz to further explain the electrochemical performances.

Results and discussion

Scheme 1 shows the procedure of synthesizing NR@CeO_2 samples, involving two hydrothermal treatment steps. At the first hydrothermal process at 100 °C for 24 h, some Ce^{3+} ions in NaOH solution can be oxidized to Ce^{4+} ions, forming a mixture of $Ce(OH)_3$ and CeO_2 nanorods after centrifugation. In the following step, with continuous reaction in the stainless autoclave at different temperatures, the $Ce(OH)_3$ and CeO_2 nanorods of various content of oxygen vacancies will be acquired. This is due to the fact that some oxygen atoms in the crystal structure of CeO_2 can be lost and result in defects during the hydrothermal treatment process. The number of oxygen defects vary with the change of temperature. Therefore, we finally fabricated CeO_2 cathode LOBs with different oxygen vacancies.

From the SEM images of Ce@120, Ce@160 and Ce@200 in Figure 1(a), Figure S1(a) and (c), CeO_2 catalysts show one-dimensional morphology and uneven surface. Figure 1(b)-(d), Figure S1(b) and (d) show TEM and HR-TEM micrographs of NR@CeO_2 synthesized by the above hydrothermal treatment. The average width of NR@CeO_2 is about 6 nm and their average length is various. Compared with the NR@CeO_2 images of Ce@120 (Figure S1(b)) and Ce@200 (Figure S1(d)), we found that the Ce@160 (Figure 1(b)) nanorods exhibit more regular arrays. In Figure 1(d), the HR-TEM images illustrated that the exposed crystal faces of NR@CeO_2 are (111) and (200) faces, possessing good stability even if severe deviation of architectures occurs.[32] The selected area electron diffraction (SAED) pattern in Figure 1(c) presents that the diffraction rings correspond to the (111), (200), (220), (311), (331) and (422) planes of Ce@160, indicating that the fabricated NR@CeO_2 are polycrystals. The X-ray diffraction (XRD) patterns of different NR@CeO_2 samples are shown in Figure 1(e), and the peaks assigned to (111), (200), (220), (311), (222), (400), (331), (420) and (422) faces of cubic CeO_2 are located at 28.55°, 33.08°, 47.48°, 56.34°, 59.09°, 69.42°, 76.70°, 79.08° and 88.43°, respectively. It demonstrates the formation of CeO_2 cubic phase (PDF#43-1002), which matches well with the SAED results.

Aiming at analysing the porous structure of the synthesized samples, N_2 adsorption-desorption isotherms of Ce@160 were collected, and shown in Figure 1(f)-(g). BET surface areas of 135.89 m^2 g^{-1} were obtained for the nanorods. It shows the characteristics of type-IV N_2 isotherms in terms of the International Union of Pure and Applied Chemistry (IUPAC) classification.[45] These results underlined the relatively high available surface area of the hybrid, suggesting numerous active sites for ORR and OER. Moreover, Ce@160 nanorods show a pore size distribution notably skewed to micro-pore diameters (Figure 1(g)). The average pore diameters are occupied under 2 nm and intensively at 1.59 nm. The formation of these micro-pores in the CeO_2 samples can be attributed to the release of oxygen during the second hydrothermal step. CeO_2 nanorods without micro-pores were obtained after the first step of the reaction, and the precursor was proved to be the mixture of $Ce(OH)_3/CeO_2$.[46, 47] However, the above mixture in the autoclave was under high pressure and temperature, which can enable its $Ce(OH)_3$ content to be transformed into Ce_2O_3 and CeO_2 by decomposition/dehydration during the second step of hydrothermal process. This process would release some water vapour and oxygen to form some micro-pores in the CeO_2 nanorods. The presence of micro-pores in Ce@160 nanorods are beneficial to facilitating O_2 and electrolyte diffusion, which could boost the mass transport and thus result in remarkably enhanced LOBs performance.

To evaluate the content of oxygen vacancies in NR@CeO_2 samples, we employed Raman spectroscopy to compare the

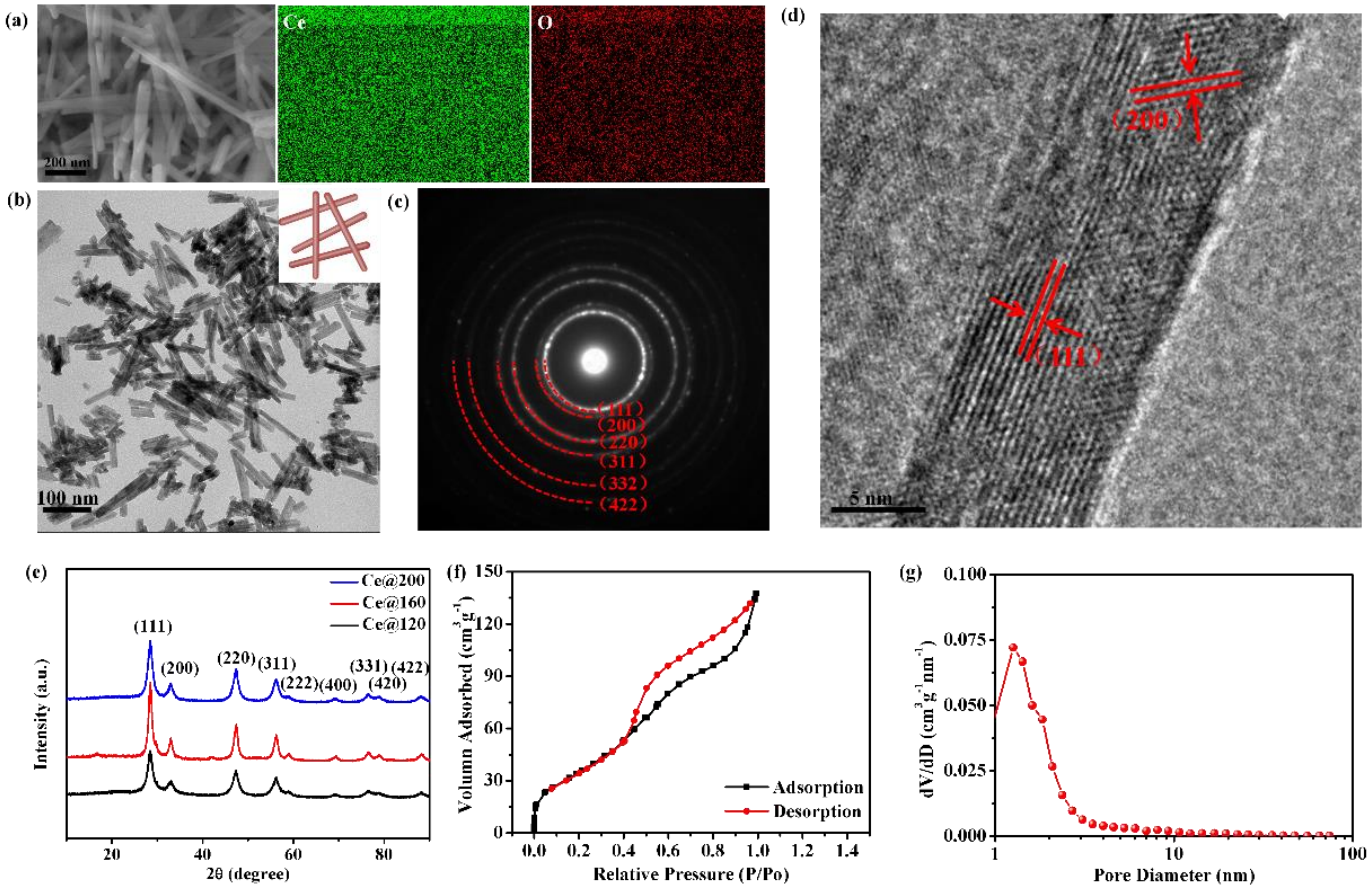

Figure 1. SEM images and the corresponding EDS pattern of Ce and O in Ce@160 nanorods**(a)**; TEM and HRTEM images of the Ce@160 nanorods**(b)**, **(d)**; and the corresponding SAED pattern**(c)**. The X-ray diffraction (XRD) patterns of different NR@CeO_2 samples**(e)**; Nitrogen adsorption-desorption isotherm loop**(f)** and pore size distribution curve**(g)** calculated from the desorption branch by using the BJH model of Ce@160.

contents of oxygen vacancies between these samples in Figure 2(a) and (b). The Raman shift peak at 459 cm^{-1} belongs to the symmetrical stretching mode of the fluorite crystal unit and the peak at 600 cm^{-1} is ascribed to the existence of oxygen vacancies in the CeO_2 lattice.[48] The concentration of oxygen vacancy can be quantified by calculating the ratio of the integral peak areas at 600 and 459 cm^{-1} (A600/A459).[49] As exhibited in Figure 2(b), the A600/A459 values of Ce@120, Ce@160 and Ce@200 are 0.05, 0.25 and 0.18, respectively, illustrating that Ce@160 has the highest content of oxygen vacancy. The XPS spectra in Figure 2(c)-(e) presented the surface electron states of Ce@160 nanorods, and the peaks locating at 531.8 and 900 eV in survey spectra for three samples (Figure 2(c), Figure S2(a) and Figure S3(a)), corresponding to the signals of O 1s and Ce 3d. The higher solution Ce 3d spectra of different samples were presented in Figure 2(d), Figure S2(b) and Figure S3(b), respectively. Eight peaks were fitted in the Ce 3d high-resolution XPS spectrum, among which two characteristic peaks labelled u' and v' are associated with the signals of Ce^{3+}, and the other peaks labelled u''', u'', u, v'' and v are related to the signals of Ce^{4+}.[50] These results confirmed the conclusion that the CeO_2 nanorods were successfully fabricated. By fitting the curve area in Figure 2(f), the results demonstrated that the contents of Ce^{3+} in Ce@120, Ce@160 and Ce@200 are 20%, 30% and 25%, respectively. The highest Ce^{3+} content in Ce@160 resulted in the best specific capacity performance due to the rapid conversion between Ce^{3+} and Ce^{4+} during the ORR and OER process. The presence of Ce^{3+} and Ce^{4+} would provide enough active sites for the adsorption and reduction of oxygen during the discharge and charge process, which is proposed as the following reaction equations (1)-(2):

$$CeO_2 \rightarrow CeO_{2-X} + (x/2)O_2 \quad (1)$$

$$nCeO_{2-X} + O_2 \rightarrow nCeO_{2-X} + O_2^- \rightarrow [n\,CeO_{2-X}]^{2+} + O_2^{2-} \quad (2)$$

The high-resolution O1s spectrum in Figure 2(e), Figure S2(c) and Figure S3(c), can be fitted into three individual component peaks located at about 529.9, 531.8 and 532.6 eV, which can be ascribed to CeO_2 (Ce 3d-O 2p bond), defect sites (oxygen vacancies) and molecular water absorbed in the samples or on their surface, respectively.[20, 51] Figure 2(f) shows the contents of oxygen vacancy in three samples, indicating that the concentration of oxygen vacancies could be controlled through regulating the hydrothermal temperature. The highest concentration of oxygen vacancy can also be seen in the data of Ce@160 nanorods, the results of which is corresponding to A600/A459 results in Figure 2(b).

To explore the mechanism of oxygen vacancy on catalysing the electrochemical process of LOBs, we assembled the lithium oxygen cells using the CeO_2 nanorods of different contents of oxygen vacancy as cathode and then measured their

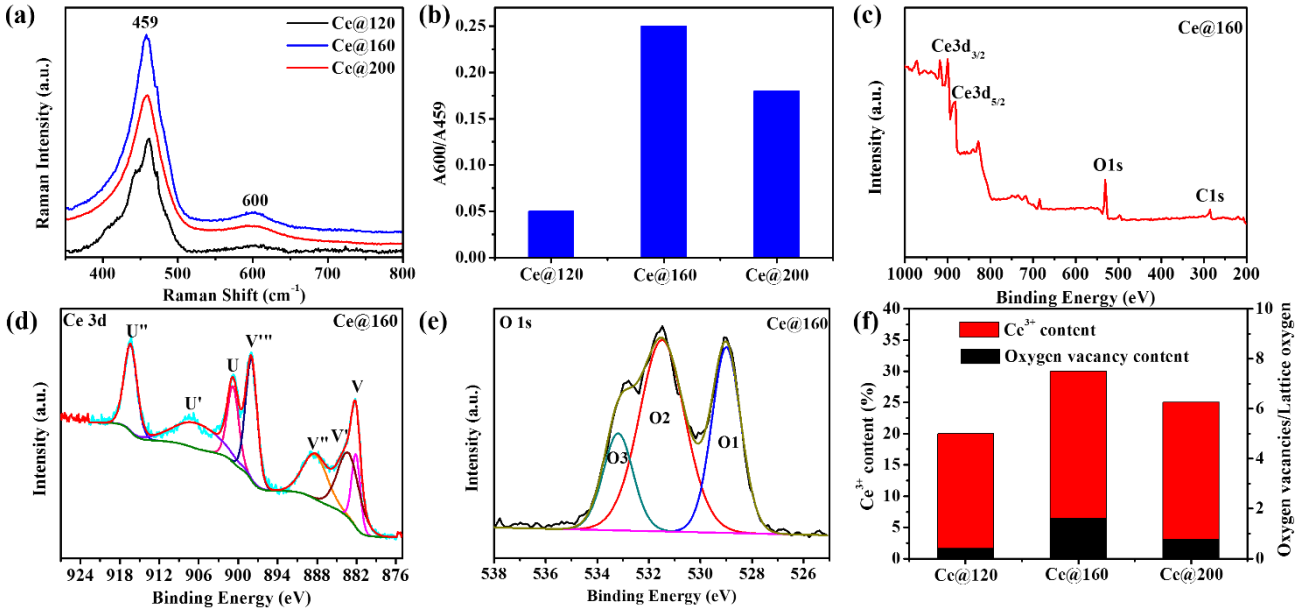

Figure 2. Raman spectra of different NR@CeO_2 samples**(a)** and the ratio of the integrated peak areas under the bands at 600 and 459 cm^{-1} of NR@CeO_2**(b)**; high-resolution XPS spectra of Ce@160 for survey curve**(c)**, Ce 3d**(d)** and O 1s**(e)**; and the comparison of oxygen vacancy concentration and Ce^{3+} content between different samples**(f)**.

specific capacities between 2.35 to 4.5 V (vs. Li/Li^+). The results are recorded in Figure 3(a)-(b). The Ce@160 cathode delivered the highest discharge/charge capacities of 11775/11683 mAh g^{-1} at a current density of 100 mA g^{-1}, while the Ce@120 and Ce@200 cathodes show those of 7017/5971 and 7292/5816 mAh g^{-1}, respectively. When contrasted the deviation of the assembled cells, these results illustrate that with the highest concentration of oxygen vacancies, the Ce@160 cathode shows the largest discharge/charge capacities. In Figure 3(b), all the batteries show high Columbic efficiencies of 99.7%, 96.1%, 88.7%, 78.8% and 80.2% at varied current batteries, which illustrated that the extraordinary reversibility and rate capability of Ce@160 cathode can be attributed to the existence of oxygen vacancies. This can accelerate electron conductivity in the Li_2O_2 films and thus contribute to decompose Li_2O_2 films. The current and specific capacities were calculated on the basis of the average weight of the cathode material in order to utilize the same testing conditions. Obviously, the capacity of the carbon paper in Figure S4 was quite limited, which is only less than 400 mAh g^{-1} at a current density of 100 mA g^{-1}, indicating that the carbon paper contributes negligibly to the catalyst specific capacity and it is reasonable to use carbon paper as the current collector in the research on LOBs. To further investigate the electrocatalytic effect for different contents of oxygen vacancy, Ce@120, Ce@160 and Ce@200 samples were both carried out cyclic performance measurements. The cycling performance of the Ce@160 cathode with the fixed capacities of 600 and 1000 mAh g^{-1} at a current density of 100 mA g^{-1} were shown in Figure 3(d)-(h), and that of Ce@120 and Ce@200 cathode were shown in Figure S5. The Ce@160 cathode could be galvanostatically cycled for 200 and 70 cycles at the limited specific capacity of 600 and 1000 mAh g^{-1}, respectively. In contrast, the cycle life for Ce@120 cathode and Ce@120 cathode with a capacity cut-off of 600 mA h g^{-1} were just 33 cycles and 45 cycles, respectively. The best electrochemical performance for Ce@160 cathode LOBs can be attributed to the highest content of oxygen vacancy, because the more oxygen vacancies could induce more active sites for promoting the ORR and OER reaction.

Ex-situ XPS was used to further explore the reaction mechanisms for the Ce@160 cathode during the discharge and charge process at a current density of 100 mA g^{-1}, as presented in Figure 4(b)-(i), in accordance with states 1-4 in Figure 4(a). Figure 4(b)-(e) show the evolution process of the discharge products at the four states. The Li 1s XPS signals of the initial discharge process in Figure 4(b) illustrate that $Li_{2-x}O_2$(~56.1 eV) is the major discharge product and Li_2O_2(~54.5 eV) is also produced through the further reaction between $Li_{2-x}O_2$ and O_2 at the state 1.[30, 52, 53] After the cathode was fully discharged to 2.35 V(state 2), the peak of $Li_{2-x}O_2$ vanishes and the concentration of Li_2O_2 exhibits an obvious increase in Figure 4(c), which can be attributed to the deposition of Li_2O_2 on the surface of the LiO_2 or the disproportionation of LiO_2. More interestingly, we found that the signals related to $Li_{2-x}O_2$ reappear in Figure 4(d) during the initial charging process (state 3), suggesting the presence of intermediate discharge product $Li_{2-x}O_2$. Figure 4(e) presented Li 1 s XPS signals detected after fully recharged to 4.5 V (state 4), and we can imply that the discharge products Li_2O_2 can be reversibly decomposed through NR@CeO_2 because of the disappearance of Li 1s signals. In addition, the O 1s XPS signals were also investigated to illustrate the role of oxygen vacancy playing in the discharge and charge process, and the peak at 533 and 531.5 eV can be ascribed to hydroxyl species and oxygen vacancies, respectively.[20] The concentration of oxygen vacancies

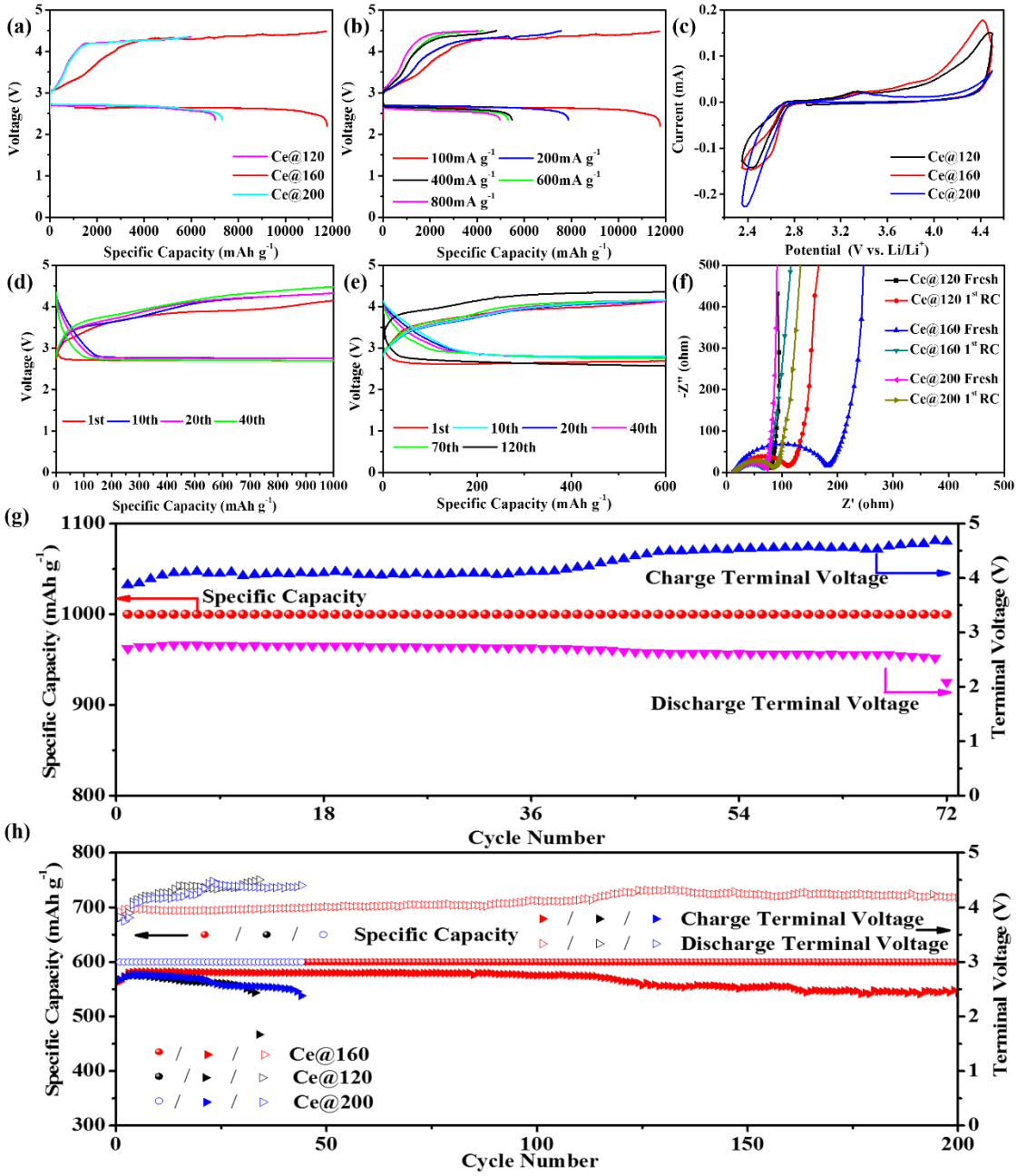

Figure 3. Comparison of the initial discharge/charge profiles of the LOBs from 2.35 to 4.5 V for Ce@120, Ce@160 and Ce@200 cathode at 100 mAh g^{-1}**(a)**; and Ce@160 cathode at different current densities**(b)**; CV curves of different samples at 0.1 $mV \cdot s^{-1}$ between 2.35 and 4.5 V**(c)**; EIS spectrums of different samples electrodes before and after recharge**(f)**; cycling performances (**(g)** and **(h)**), and the corresponding typical discharge/charge profiles (**(d)** and **(e)**) of the LOBs for selected cycles, with (**(d)**, **(g)**) and (**(e)**, **(h)**) the profiles of the Ce@160 cathode under a specific capacity limit of 600 mAh g^{-1} at 100 mA g^{-1} and under a specific capacity limit of 1000 mAh g^{-1} at 100 mA g^{-1}, respectively.

decreases from 54.25% to 8.39% after the cathode was fully discharged to 2.35 V(state 2), and climbs to 52.93%(which is close to the concentration of state 1) after the cathode was fully recharged to 4.5 V(state 4). The changing concentration of oxygen vacancies in the cathode suggest that the oxygen vacancies of CeO_2 nanorods have more obviously positive effects on ORR than OER, including lowering the overpotential of ORR from 0.26 V to 0.11 V, and also prolonging the cycle life of LOBs, because oxygen vacancies can facilitate the electron transport through Li_2O_2 films to catalyse the reaction between Li^+ and O_2 during both discharge and charge process. It is worth noting that oxygen vacancies can also catalyse the deposition of Li_2O_2 films as the active sites, which could be involved in the reaction between Li^+ and O_2 during discharge process.

These results imply that the high-concentration oxygen vacancy on the CeO_2 nanorods effectively diminish the reaction energy barrier of ORR and OER during the discharge and charge process, which was proposed by Zhang et. al. that the deteriorating electron transportation through the previously formed Li_2O_2 films can result in the sudden termination of discharge reaction and the limitation of charge reaction.[7, 54] As oxygen vacancies can bring enhancement to the transmission of electron and attend ORR between Li^+ and O_2 to form Li_2O_2, the Ce@160 can achieve the most satisfying electrochemical performance owing to the highest content of oxygen vacancies. It is believed that they can serve as the active sites to the deposition of Li_2O_2 films by being involved in the reaction between Li^+ and O_2 during ORR, and also boost the electron transport through the insoluble Li_2O_2 films to further catalyze the Li^+ and O_2 reaction during discharge and charge process. In Figure 3(h), it was found that the first 100 cycles were quite stable with an average discharge plateau of 2.8 V and a charge plateau of 4.0 V, demonstrating a relatively low potential gap of 1.2 V. The comparatively low over-potential and stable cycling performance of the first dozens of cycles could be due to the catalytic effects caused by oxygen vacancies in Ce@160 nanorods, which contributed effectively to the adsorption and conversion of O_2 and Li_2O_2. However, the increased over-potentials of following cycles may be attributed to the fact that the cycle mode with limited capacity and unspaced time after each discharge and charge step, resulting in residual polarization.

To explore the kinetic electrochemical behaviours of Ce@160 cathode, CV tests were conducted for different samples at 0.1 mV s^{-1} scan rate, as shown in Figure 3(c). Ce@160 cathode displayed stronger peaks and lower over-potential, compared to those of Ce@120 and Ce@200 cathodes. As can be seen in the CV curves of Ce@160 cathode, one reduction peak was found at 2.50 V for ORR process, and two anodic peaks appeared at around 3.37 V and 4.41 V for OER process, respectively. The only one reduction peak at 2.50 V represented the generation of Li_2O_2 films from the reaction between Li^+ and O_2 adsorbed on the oxygen vacancies.[55] The oxidation peak at 3.37 V can be ascribed to the formation of intermediate product Li_2O, which was produced through the disproportionation of Li_2O_2 with the release of Li^+ and O_2.[56] In

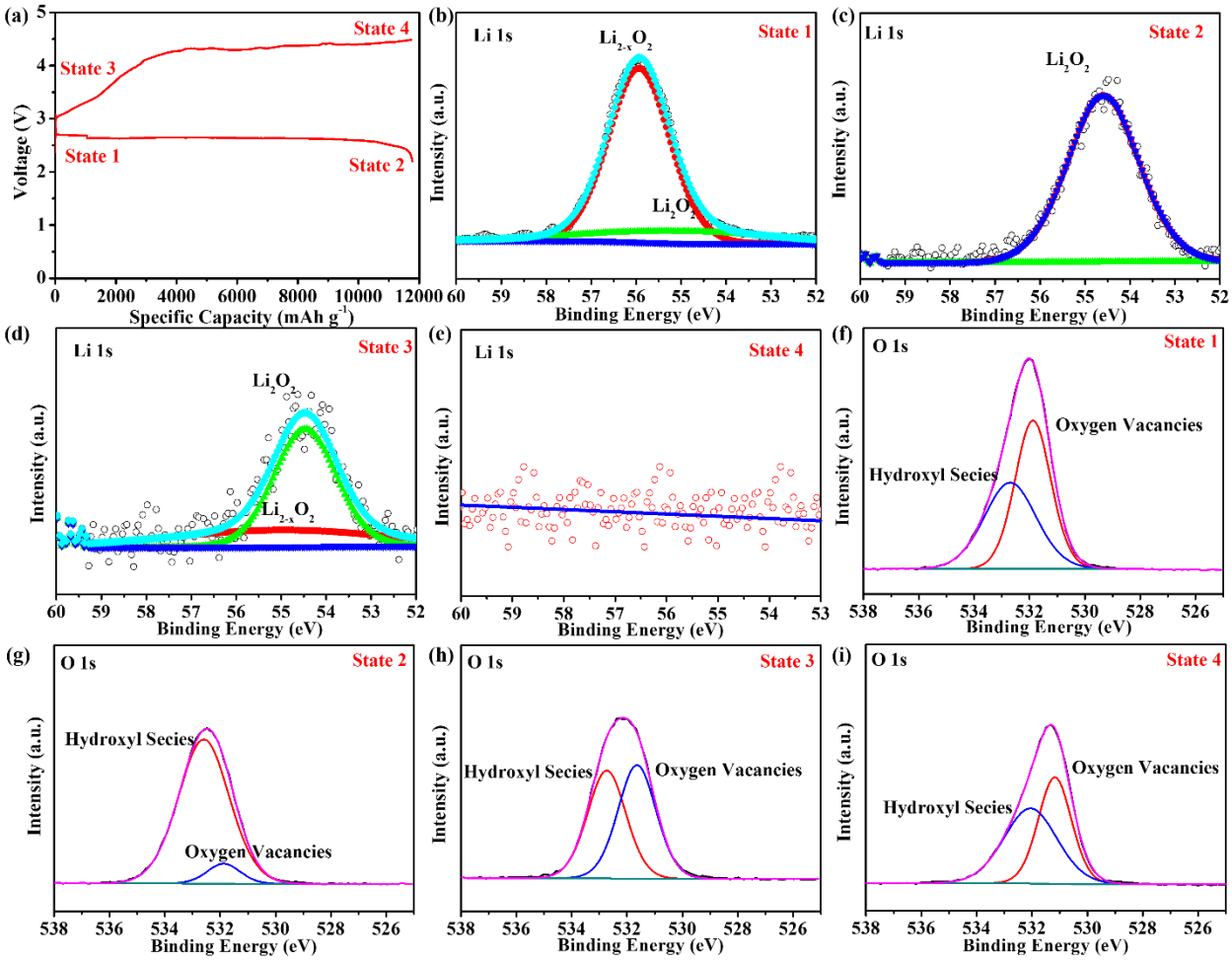

Figure 4. Reaction mechanisms for the Ce@160 cathode during the discharge and charge process: the discharge-charge behavior of cathode at a current density of 100 mA g^{-1}**(a)**; high-resolution XPS spectra of the Li 1s of Ce@160 nanorods cathode**(b)-(e)**; and high-resolution XPS spectra of the O 1s of Ce@160 nanorods cathode**(f)-(i)** at different states in the 2th cycle, corresponding to points(1-4) in**(a)**, respectively.

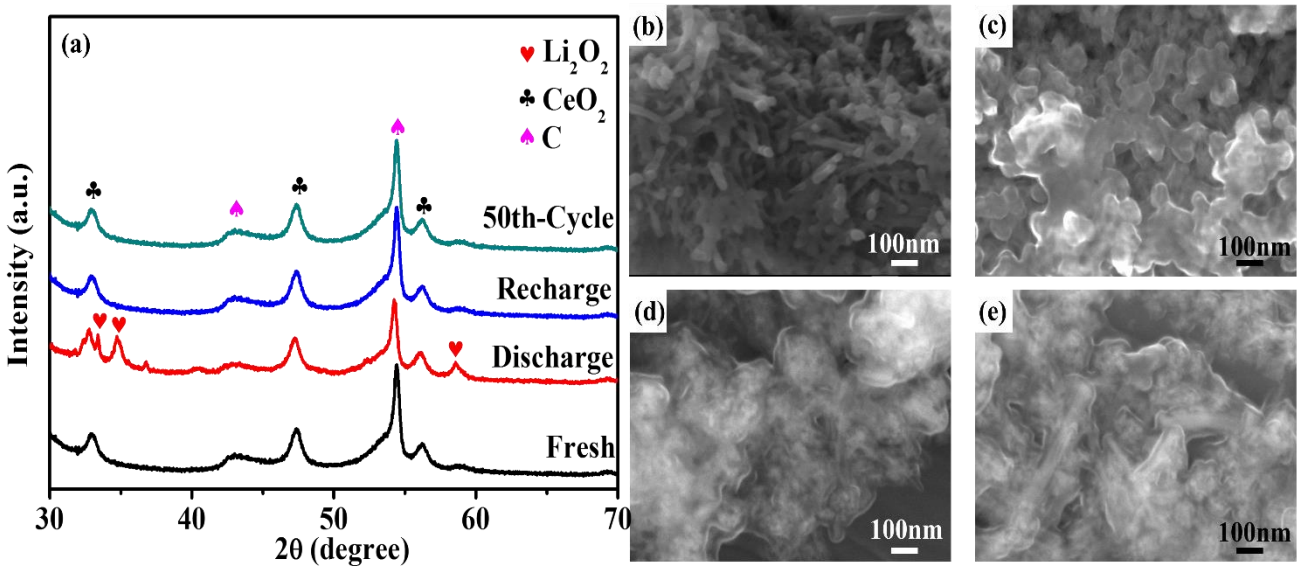

Figure 5. Structure and composition characterization of products at different stage: XRD patterns at different discharge/charge stages**(a)**; and FE-SEM images of Ce@160 nanorods cathodes at the fresh stage**(b)**, the 1st cycle, fully discharged (to 2.35 V)**(c)**, the 1st cycle, fully charged (to 4.5 V)**(d)**, and after 50 cycles fixed specific capacity charging**(e)**.

addition, the peak at 4.41 V was assigned to further delithiation of bulk Li_2O_2.[2, 52, 57] As the results observed above, the Ce@160 cathode displays the largest current value and the lowest over-potential, compared with those of another two samples. This indicated that Ce@160 could improve the Li_2O_2-oxidation kinetics and thus lead to improved battery efficiency. To further explain the performance of the LOB during cycling, EIS was applied at open circuit voltage (OCV) within a frequency range of 10^5 to 0.1 Hz at the pristine stage and at the end of the first recharge processes (Figure 3(f)). The charge transfer resistance (R_{ct}) represented by the depressed semicircles in the middle of the frequency range can be evaluated by the diameter of the semicircle.[58] As shown in Figure 3(f), the R_{ct} of Ce@160 electrode at fresh state and recharged state were about 200 Ω and 70 Ω, respectively. The R_{ct} of Ce@160 electrode became smaller after recharging, and the behaviour of which presented a striking contrast to those of Ce@120 and Ce@200 electrodes. It can be concluded that the low R_{ct} of Ce@160 electrode might be attributed to its favourable reversibility, because the existence of oxygen vacancies can serve as active sites and take a catalytic part in enhancing the electron and mass transport, which extraordinarily contribute to efficiently accelerating the reaction between Li^+ and O_2. Thus, it is supposed that Ce@160 cathode shows superior ability to promote the decomposition of the discharge products with abundant contents of oxygen vacancy.

The XRD patterns of LOB with Ce@160 cathode at a fresh, 1st discharged, 1st charged and after 50th-charged stages with the limited capacity of 600 mAh g^{-1} at the current density of 100 mA g^{-1} in Figure 5(a) were used to explore the component changes during cycling. The characteristic Li_2O_2 peaks can be distinctly observed in the cathode after the 1st full discharging, and the they were not found in the XRD patterns of the cathodes after the subsequent charging and after the 50th fixed specific capacity charging stages, illustrating that the CeO_2 nanorod cathode could efficiently catalyse the formation and decomposition of the Li_2O_2. A few insoluble by-products have been produced during cycling, based on the XPS results in Figure 4(b)-(e). The CeO_2 nanorods can be observed clearly on the fresh electrode in Figure 5(b). After discharging, some Li_2O_2 films had formed, and each edge on the surface of nanorod had become quite rough in Figure 5(c). However, in Figure 5(d) and (e), the Li_2O_2 films were partly eliminated after 1st recharged and 50 recharged stages with the limited capacity of 600 mAh g^{-1} at the current density of 100 mA g^{-1}, which may be attributed to the satisfying electrocatalytic ability of CeO_2

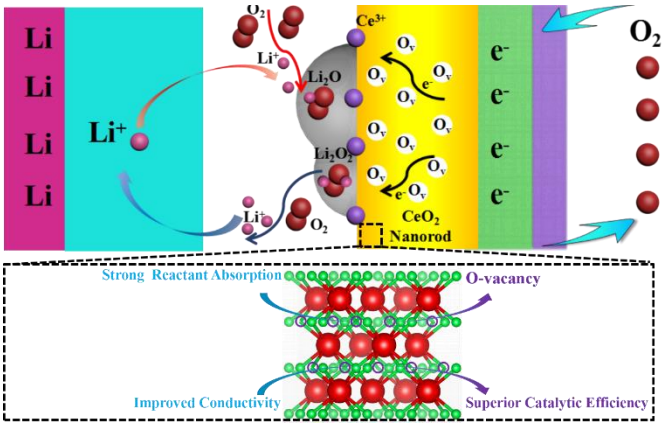

Scheme 2. Schematic representation of the proposed electrochemical mechanism of the reversible formation of the discharge products on the surface oxygen vacancies of CeO_2 nanorod cathode.

nanorods during the OER process. It is worth noting that CeO_2 nanorods can play a significant part in the adsorption and decomposition of Li_2O_2 films during the ORR and OER process, and the catalytic ability can be significantly enhanced by tuning oxygen vacancies to the most appropriate content.

The superior electro-catalytic performance of Ce@160 according to specific capacity, rate capability and long cycle life could be ascribed to its high contents of oxygen vacancy, as shown in Scheme 2. The existence of abundant oxygen vacancies was crucial to enhance Li^+ and electron transport behaviour because oxygen vacancies can diminish the energy barrier of electron transport through insoluble Li_2O_2 films. This could further boost the reaction between Li^+ and O_2 during discharge process, and enable Li_2O_2 films decompose efficiently. It also can significantly enhance the intrinsic conductivity and provide more active sites for ORR and OER, which is also helpful for optimizing the electrochemical performance of Ce@160 cathode.[20]

Conclusions

To investigate the electrocatalytic effect of different oxygen vacancy concentration of CeO_2 nanorods for LOBs, we successfully used two-step hydrothermal method to tune the contents of oxygen vacancy in CeO_2 nanorods. The Ce@160 cathode exhibited the best electrochemical performance due to its highest amount of oxygen vacancies. This Ce@160 cathode delivered extraordinary rate capability, high specific capacity of 12000 mAh g^{-1} and stable cycle stability of about 200 cycles. The reason for the advanced electrochemical performance was that oxygen vacancies of Ce@160 can not only contribute effectively to improving the adsorption and conversion of O_2 and Li_2O_2 during discharge and charge process, but also can serve as active sites for ORR. These could enable optimized reaction pathway for the CeO_2 nanorod cathode, and excellent electrode stability with superior catalytic efficiency could be achieved. Therefore, it is concluded that high content of oxygen vacancy can be beneficial to improve electrocatalytic ability of CeO_2 nanorods and enhance electrochemical performances in LOBs, giving a controllable and efficient strategy for boosting the electrochemical performances of other metal oxides materials as cathodes for LOBs.

Conflicts of interest

There are no conflicts to declare.

Acknowledgements

This work was supported by Qilu Young Scholar Program in Shandong University, Open Program in Tsinghua University State Key Laboratory of New Ceramic and Fine Processing (KF201814, KF201805), Open Program in Guangxi Key Laboratory of Information Materials (171002-K)

Notes and references

1. C. Hou, Z. Tai, L. Zhao, Y. Zhai, Y. Hou, Y. Fan, F. Dang, J. Wang and H. Liu, *J. Mater. Chem. A*, 2018, **6**, 9723-9736.
2. Y. Lu, B. M. Gallant, D. G. Kwabi, J. R. Harding, R. R. Mitchell, M. S. Whittingham and Y. S. Horn, *Energy Environ. Sci.*, 2013, **6**, 750-768.
3. K. N. Jung, J. Kim, Y. Yamauchi, M. S. Park, J. W. Lee and J. H. Kim, *J. Mater. Chem. A*, 2016, **4**, 14050-14068.
4. Q. Xu, W. Lei, X. Li, X. Qi, J. G. Yu, G. Liu, J. Wang and P. Zhang, *Environ. Sci. Technol.*, 2014, **48**, 9702-9708.
5. Y. Zhang, M. Li, B. Hua, Y. Wang, Y. Suna and J. Luo, *Appl. Cata. B: Environmental*, 2018, **236**, 413-419.
6. A. Kraytsberg and Y. E. Eli, *J. Power Sources*, 2011, **196**, 886-893.
7. Z. Peng, S. A. Freunberger, Y. Chen and P. G. Bruce, *Science* 2012, **337**, 563-566.
8. J. Wang, L. Liu, S. Chou, H. Liub and J. Wang, *J. Mater. Chem. A*, 2017, **5**, 1462-1471.
9. M. N. Samani, H. D. Lim, S. Haghighat Shishavan, H. K. Kim, Y. M. Ko, M. S. Kim, S. W. Lee, S. F. Kashani Bozorg, M. Abbasi, H. U. Guim, D. I. Kim, K. C. Roh, K. Kang and K. B. Kim, *J. Mater. Chem. A*, 2017, **5**, 619-631.
10. L. Leng, J. Li, X. Zeng, H. Song, T. Shu, H. Wang and S. Liao, *J. Power Sources*, 2017, **337**, 173-179.
11. X. Ren, M. Huang, S. Luo, Y. Li, L. Deng, H. Mi, L. Sun and P. Zhang, *J. Mater. Chem. A*, 2018, **6**, 10856-10867.
12. Y. Gong, W. Ding, Z. Li, R. Su, X. Zhang, J. Wang, J. Zhou, Z. Wang, Y. Gao, S. Li, P. Guan, Z. Wei and C. Sun, *ACS Catal.*, 2018, **8**, 4082-4090.
13. R. Gao, Z. Yang, L. Zheng, L. Gu, L. Liu, Y. Lee, Z. Hu and X. Liu, *ACS Cata.*, 2018, **8**, 1955-1963.
14. X. Zhang, Y. Gong, S. Li and C. Sun, *ACS Cata.*, 2017, **7**, 7737-7747.
15. W. Yang, Z. Qian, C. Du, C. Hua, P. Zuo, X. Cheng, Y. Ma and G. Yin, *Carbon*, 2017, **118**, 139-147.
16. J. Luo, X. Yao, L. Yang, Y. Han, L. Chen, X. Geng, V. Vattipalli, Q. Dong, W. Fan, D. Wang and H. Zhu, *Nano Research*, 2017, **10**, 4318-4326.
17. B. Sun, K. Kretschmer, X. Xie, P. Munroe, Z. Peng and G. Wang, *Adv. Mater.*, 2017, **29**, 1606816.
18. Y. Ji, H. Dong, T. Hou and Y. Li, *J. Mater. Chem. A*, 2018, **6**, 2212-2218.
19. Q. Zhu, S. Xu, M. Harris, C. Ma, Y. Liu, X. Wei, H. Xu, Y. Zhou, Y. Cao, K. Wang and J. Chen, *Adv. Funct. Mater.*, 2016, **26**, 8514-8520.
20. C. Hou, Y. Hou, Y. Fan, Y. Zhai, Y. Wang, Z. Sun, R. Fan, F. Dang and J. Wang, *J. Mater. Chem. A*, 2018, **6**, 6967-6976.
21. Y. Jia, L. Zhang, A. Du, G. Gao, J. Chen, X. Yan, C. L. Brown and X. Yao, *Adv. Mater.*, 2016, **28**, 9532-9538.
22. L. Leng, X. Zeng, H. Song, T. Shu, H. Wang and S. Liao, *J. Mater. Chem. A*, 2015, **3**, 15626-15632.
23. J. Wang, R. Gao, D. Zhou, Z. Chen, Z. Wu, G. Schumacher, Z. Hu and X. Liu, *ACS Cata.*, 2017, **7**,

6533-6541.
24. J. Zhang, P. Li, Z. Wang, J. Qiao, D. Rooney, W. Sun and K. Sun, *J. Mater. Chem. A*, 2015, **3**, 1504-1510.
25. J. Zhu, F. Wang, B. Wang, Y. Wang, J. Liu, W. Zhang and Z. Wen, *J. Am. Chem. Soc.*, 2015, **137**, 13572-13579.
26. J. Bao, X. Zhang, B. Fan, J. Zhang, M. Zhou, W. Yang, X. Hu, H. Wang, B. Pan and Y. Xie, *Angew. Chem. Int. Ed.* , 2015, **54**, 7399-7404.
27. H. Lin, N. Liu, Z. Shi, Y. Guo, Y. Tang and Q. Gao, *Adv. Funct. Mater.*, 2016, **26**, 5590-5598.
28. K. Song, E. Cho and Y. M. Kang, *ACS Cata.*, 2015, **5**, 5116-5122.
29. S. Chen, J. Duan, A. Vasileff and Q. Zhang, *Angew. Chem. Int. Ed.*, 2016, **55**, 3804-3808
30. S. Zhang, G. Wang, J. Jin, L. Zhang, Z. Wen and J. Yang, *Nano Energy*, 2017, **36**, 186-196.
31. J. H. Lee, R. Black, G. Popov, E. Pomerantseva, F. Nan, G. A. Botton and L. F. Nazar, *Energy Environ. Sci.*, 2012, **5**, 9558.
32. A. Beste and S. H. Overbury, *J. Phys. Chem. C*, 2015, **119**, 2447-2455.
33. Y. B. Kim, T. P. Holme, T. M. Gür and F. B. Prinz, *Adv. Funct. Mater.*, 2011, **21**, 4684-4690.
34. C. R. Michel and A. H. Martínez-Preciado, *Sensors and Actuators B: Chemical*, 2014, **197**, 177-184.
35. Q. Zhu and Q. Xu, *Chem. Soc. Rev.*, 2014, **43**, 5468-5512.
36. C. Deng, Q. Huang, X. Zhu, Q. Hu, W. Su, J. Qian, L. Dong, B. Li, M. Fan and C. Liang, *Appl. Surface Sci.*, 2016, **389**, 1033-1049.
37. H. Li, K. Li, H. Wang, X. Zhu, Y. Wei, D. Yan, X. Cheng and K. Zhai, *Appl. Surface Sci.*, 2016, **390**, 513-525.
38. W. Cai, F. Wang, C. Daniel, A. C. van Veen, Y. Schuurman, C. Descorme, H. Provendier, W. Shen and C. Mirodatos, *J. Cata.*, 2012, **286**, 137-152.
39. J. Ke, J. W. Xiao, W. Zhu, H. Liu, R. Si, Y. W. Zhang and C. H. Yan, *J. Am. Chem. Soc.*, 2013, **135**, 15191-15200.
40. X. Lin, L. Zhou, T. Huang and A. Yu, *Int. J. Electrochem. Sci.*, 2012, **7**, 9550-9559.
41. C. H. Ahn, R. S. Kalubarme, Y. H. Kim, K. N. Jung, K. H. Shin and C. J. Park, *Electrochimi. Acta*, 2014, **117**, 18-25.
42. R. S. Kalubarme, H. S. Jadhav, C. N. Park, K. N. Jung, K. H. Shin and C. J. Park, *J. Mater. Chem. A*, 2014, **2**, 13024.
43. C. Cao, J. Xie, S. Zhang, B. Pan, G. Cao and X. Zhao, *J. Mater. Chem. A*, 2017, **5**, 6747-6755.
44. Y. Jiang, J. Cheng, L. Zou, X. Li, Y. Huang, L. Jia, B. Chi, J. Pu and J. Li, *ChemCatChem* 2017, **5**, 1-8.
45. S. Zhu, J. Li, X. Deng, C. He, E. Liu, F. He, C. Shi and N. Zhao, *Adv. Funct. Mater.*, 2017, **27**, 1605017.
46. J. Li, Z. Zhang, Z. Tian, X. Zhou, Z. Zheng, Y. Ma and Y. Qu, *J. Mater. Chem. A*, 2014, **2**, 16459-16466.
47. Z. Tian, J. Li, Z. Zhang, W. Gao, X. Zhou and Y. Qu, *Biomaterials*, 2015, **59**, 116-124.
48. S. Zhang, J. Li, W. Gao and Y. Qu, *Nanoscale*, 2015, **7**, 3016-3021.
49. M. Guo, J. Lu, Y. Wu, Y. Wang and M. Luo, *Langmuir.*, 2011, **27**, 3872-3877.
50. L. Ma, R. Chen, G. Zhu, Y. Hu, Y. Wang, T. Chen, J. Liu and Z. Jin, *ACS Nano*, 2017, **11**, 7274-7283.
51. L. Li, Y. Li, S. Gao and N. Koshizaki, *J. Mater. Chem.* , 2009, **19**, 8366-8371.
52. J. Lu, Y. J. Lee, X. Luo, K. C. Lau, M. Asadi, H. H. Wang, S. Brombosz, J. Wen, D. Zhai, Z. Chen, D. J. Miller, Y. S. Jeong, J. B. Park, Z. Z. Fang, B. Kumar, A. Salehi-Khojin, Y. K. Sun, L. A. Curtiss and K. Amine, *Nature*, 2016, **529**, 377-382.
53. K. P. C. Yao, D. G. Kwabi, R. A. Quinlan, A. N. Mansour, A. Grimaud, Y. L. Lee, Y. C. Lu and Y. Shao-Horn, *J. Electrochem. Soc.*, 2013, **160**, A824-A831.
54. Y. Zhang, Q. Cui, X. Zhang, W. C. McKee, Y. Xu, S. Ling, H. Li, G. Zhong, Y. Yang and Z. Peng, *Angew. Chem. Int. Ed.*, 2016, **55**, 10717-10721.
55. L. Zou, Y. Jiang, J. Cheng, Y. Chen, B. Chi, J. Pu and L. Jian, *Electrochim. Acta*, 2018, **262**, 97-106.
56. N. Feng, P. He and H. Zhou, *Adv. Energy Mater.*, 2016, **6**, 1502303.
57. C. M. Burke, R. Black, I. R. Kochetkov, V. Giordani, D. Addison, L. F. Nazar and B. D. McCloskey, *ACS Energy Lett.*, 2016, **1**, 747-756.
58. L. Wang, M. Ara, K. Wadumesthrige, S. Salley and K. Y. S. Ng, *J. Power Sources*, 2013, **234**, 8-15.

Supporting Information

Oxygen Vacancies Promoting the Electrocatalytic Performance of the CeO_2 Nanorods as the Cathode Materials for Li-O_2 Batteries

Yue Hou,[a,‡] Jun Wang,[a,‡] Chuanxin Hou,[a] Yuqi Fan,[b] Yanjie Zhai,[a] Hongyu Li,[a] Feng Dang,[a*] Shulei Chou,[c*]

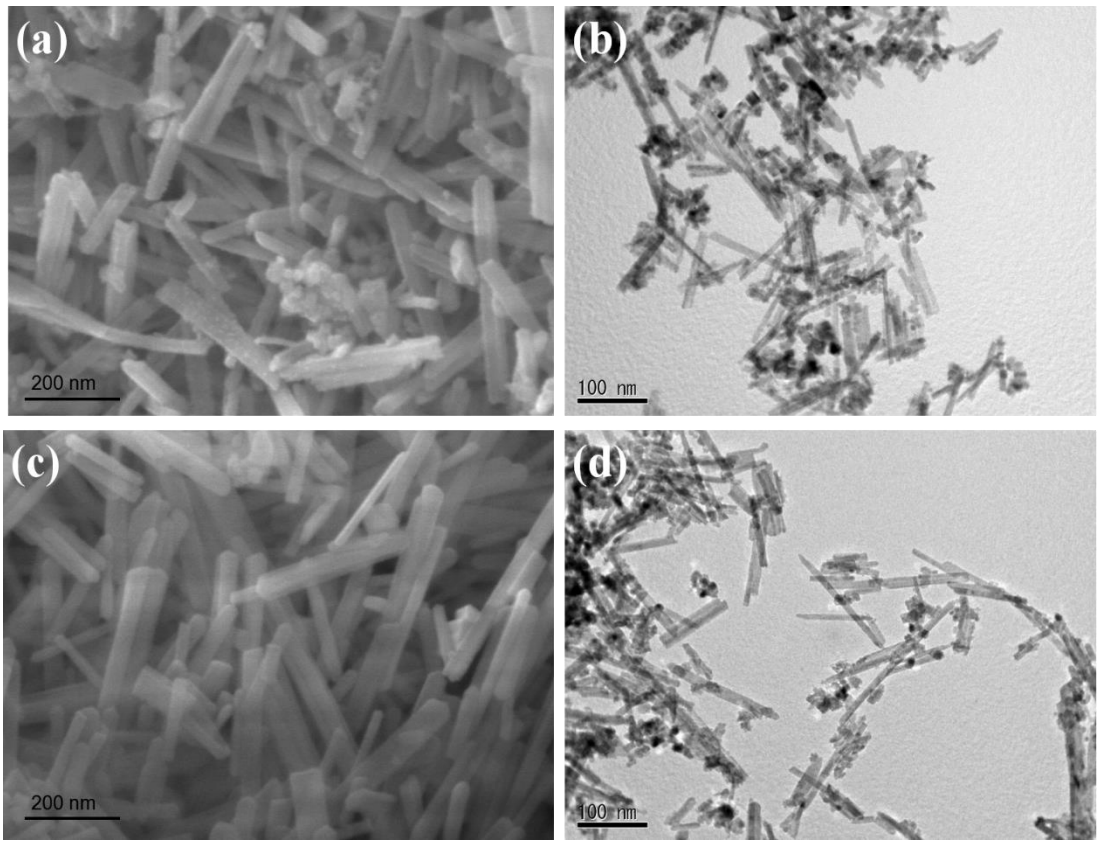

Figure S1. SEM and TEM images of Ce@120 nanorods**(a)-(b)**, and Ce@200 nanorods **(c)-(d)**.

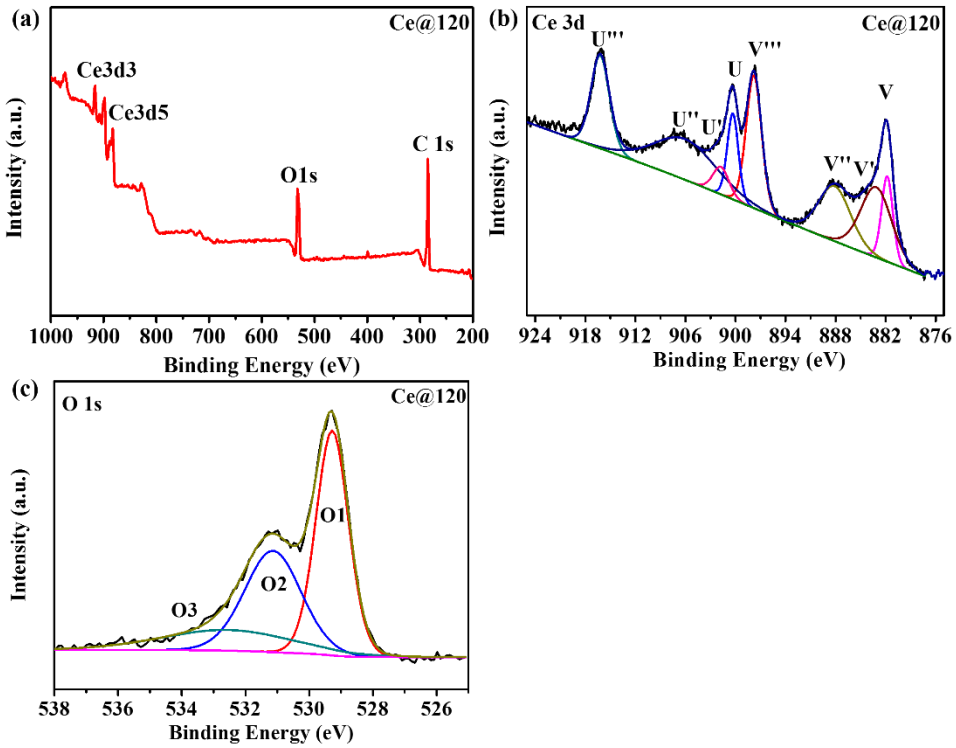

Figure S2. High-resolution XPS spectra of Ce@120 for survey curve**(a)**, Ce 3d**(b)** and O 1s**(c)**.

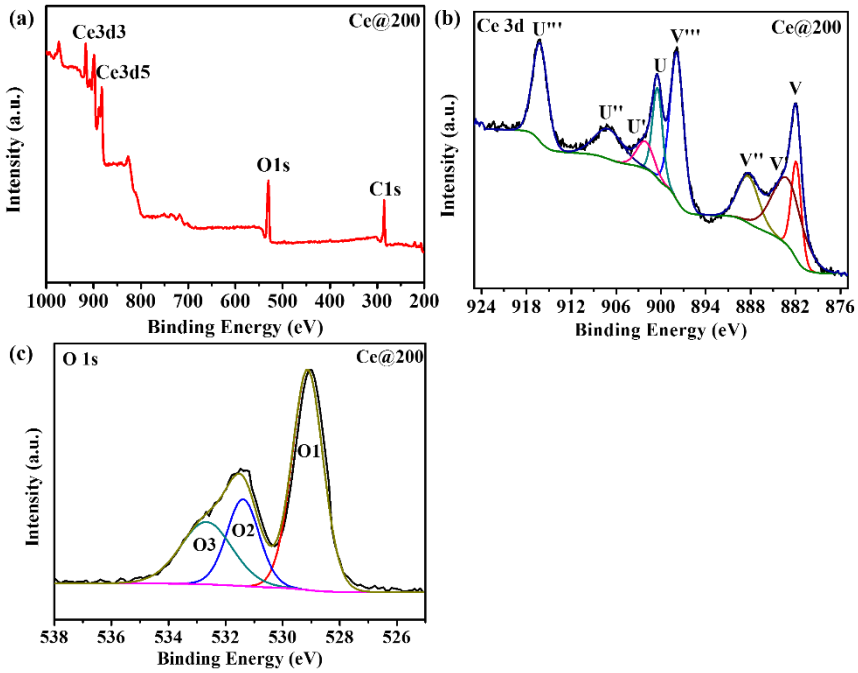

Figure S3. High-resolution XPS spectra of Ce@200 for survey curve**(a)**, Ce 3d**(b)** and O 1s**(c)**.

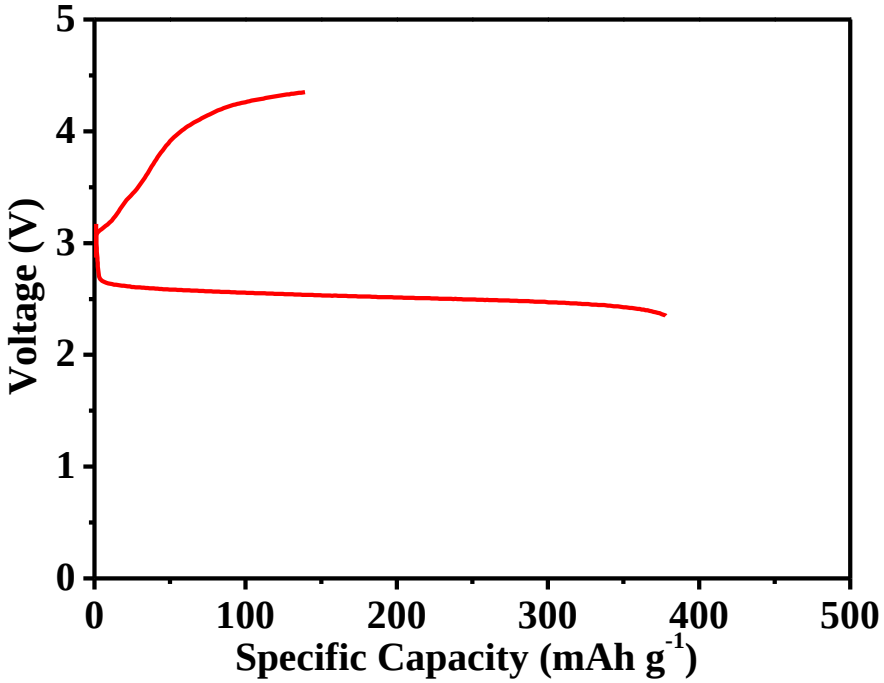

Figure S4. The initial discharge/charge profiles of the LOBs from 2.35 to 4.35 V for the pure carbon paper.

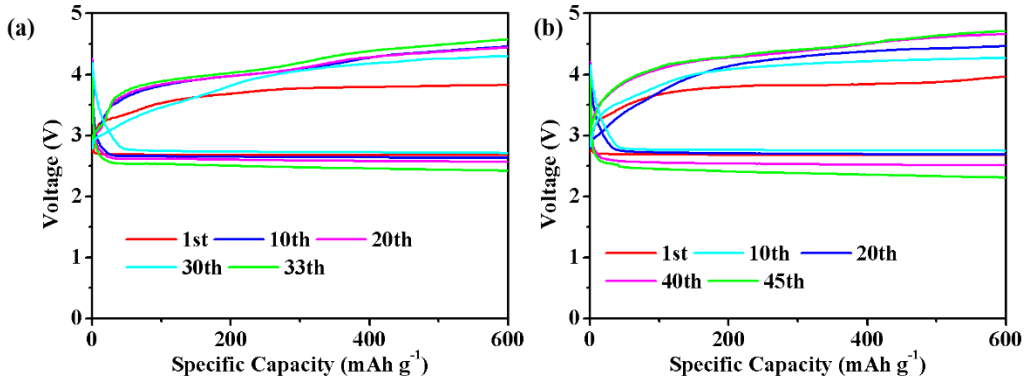

Figure S5. The corresponding typical discharge/charge profiles of the Ce@120 cathode**(a)** and the Ce@200 cathode**(b)** LOBs for selected cycles under a specific capacity limit of 600 mAh g^{-1} at 100 mA g^{-1}.